COMMUNICATIONS MATERIALS

ARTICLE

https://doi.org/10.1038/s43246-020-00086-y OPEN

Active-matrix monolithic gas sensor array based on MoS_2 thin-film transistors

Sehwan Kim[1,3], Heekyeong Park[1,3], Sooho Choo[1,3], Seongho Baek[1], Yena Kwon[1], Na Liu[1], Jeong Yong Yang[2], Cheol-Woong Yang[1✉], Geonwook Yoo[2✉] & Sunkook Kim[1✉]

Highly sensitive and system integrable gas sensors play a significant role in industry and daily life, and MoS_2 has emerged as one of the most promising two-dimensional nanomaterials for gas sensor technology. In this study, we demonstrate a scalable and monolithically integrated active-matrix gas sensor array based on large-area bilayer MoS_2 films synthesized via two-successive steps: radio-frequency magnetron sputtering and thermal sulfurization. The fabricated thin-film transistors exhibit consistent electrical performance over a few centimeters area and resulting gas sensors detect NO_2 with ultra-high sensitivity across a wide detection range, from 1 to 256 ppm. This is due to the abundant grain boundaries of the sputtered MoS_2 channel, which perform as active sites for absorption of NO_2 gas molecules. The demonstrated active-matrix gas sensor arrays display good switching capabilities and are anticipated to be readily integrated with additional circuitry for different gas sensing and monitoring applications.

[1] Department of Advanced Materials and Science Engineering, Sungkyunkwan University (SKKU), Suwon 16419, Republic of Korea. [2] School of Electronic Engineering, Soongsil University, Seoul 06978, Republic of Korea. [3] These authors contributed equally: Sehwan Kim, Heekyeong Park, Sooho Choo. ✉email: cwyang@skku.edu; gwyoo@ssu.ac.kr; seonkuk@skku.edu

Gas sensors, which allow ubiquitous and personal air-quality monitoring, pollution tracking, and preventive health care via point-of-care breath analysis, are in great demand and will become one of indispensable internet of things sensors toward the hyper-connected[1–5]. To achieve this agenda, development of low-power and monolithically integrated gas sensors without sacrificing their sensitivity is crucial, and thus various gas-sensing methods have been proposed based on electrochemical, resistive, and nanomechanical system[6–12]. In particular, chemiresistors made of semiconducting metal oxides have been extensively explored and are now the most common gas-sensing devices. These gas sensors operate in resistance modulation resulting from gas-oxide charge transfer at an elevated temperature, but they are typically bulky and require high-power consumption. In recent years, field-effect transistors (FETs) have emerged and shown a potential for overcoming the aforementioned drawbacks[13–15].

The FET-based gas sensor works on a principle of carrier transport modulation on the channel induced by gas molecules. Various nanomaterials, such as silicon nanowires, carbon nanotubes, and organic semiconductors, have been used as channel materials of the FET-based gas sensors to realize high sensitivity[16–24]. Especially, two-dimensional (2D) nanomaterials including transition metal dichalcogenides have attracted a significant attention as a promising candidate for ultrasensitive gas sensors because of a high surface-to-volume ratio and excellent charge sensitivity[25–29].

In particular, ultrahigh sensitive gas sensors based on molybdenum disulfide (MoS_2) have been successfully fabricated with mechanical and chemical exfoliation methods[30–32]. However, poor reproducibility and uniformity of exfoliated MoS_2 flakes significantly limit their practical applications. In this regard, massive efforts to grow large-area and high-crystalline MoS_2 films have been devoted, and a feasibility of diverse growth methods has been demonstrated, including chemical vapor deposition (CVD)[33,34], atomic layer deposition (ALD)[35,36], and physical vapor deposition (PVD)[37,38]. Nonetheless, the poor reliability and reproducibility of CVD owing to the unstable gas flow dynamic in the chamber as well as high-cost and low throughput of ALD reduce the availability of rather efficient and scalable growth techniques. Thus, a sputtering for large-area uniform MoS_2 films has been developed, because sputtering is a widely commercialized technique in the industry to facilitate mass-production of thin films. The sputtered MoS_2 shows large-area uniformity and good electrical properties[39,40]. However, no reports have been conducted on MoS_2 gas sensor arrays driven by large-area active-matrix.

Here, we demonstrate a scalable, highly sensitive, and monolithically integrable gas sensor active-matrix array based on bilayer MoS_2 films synthesized via a two-step method, that is, through subsequent radio-frequency (RF) magnetron sputtering and thermal sulfurization. The fabricated MoS_2 thin-film transistor (TFT)-based gas sensor exhibits a reduction of field-effect mobility (μ_{FE}) and a positive threshold voltage (V_{TH}) shift upon the exposure to nitrogen dioxide (NO_2) at room temperature, which are dissimilar to the change of exfoliated MoS_2-based gas sensors. We found that two-step-grown MoS_2 film has a polycrystalline structure and its abundant grain boundaries activate the adsorption of NO_2 molecules, resulting in the increment of potential barriers to inhibit the carrier transport in the channel. Monolithic integration of the active-matrix gas sensor array comprising switching and sensing TFTs is presented with transient gas-sensing characteristics.

Results and discussion

Characterizations of two-step-grown MoS_2. The schematic image of Fig. 1a shows the synthesis of MoS_2 film on a silicon (Si)/silicon dioxide (SiO_2) substrate, where molybdenum (Mo) metal was pre-deposited by RF magnetron sputtering at room temperature with RF power of 150 W, and then sulfurized at 750 °C in a CVD chamber with a gas mixture of hydrogen sulfide (H_2S), hydrogen (H_2), and argon (Ar). The sulfurization induced a transition from the Mo film into a layered MoS_2 structure (bottom of Fig. 1a). The thickness of Mo film, which

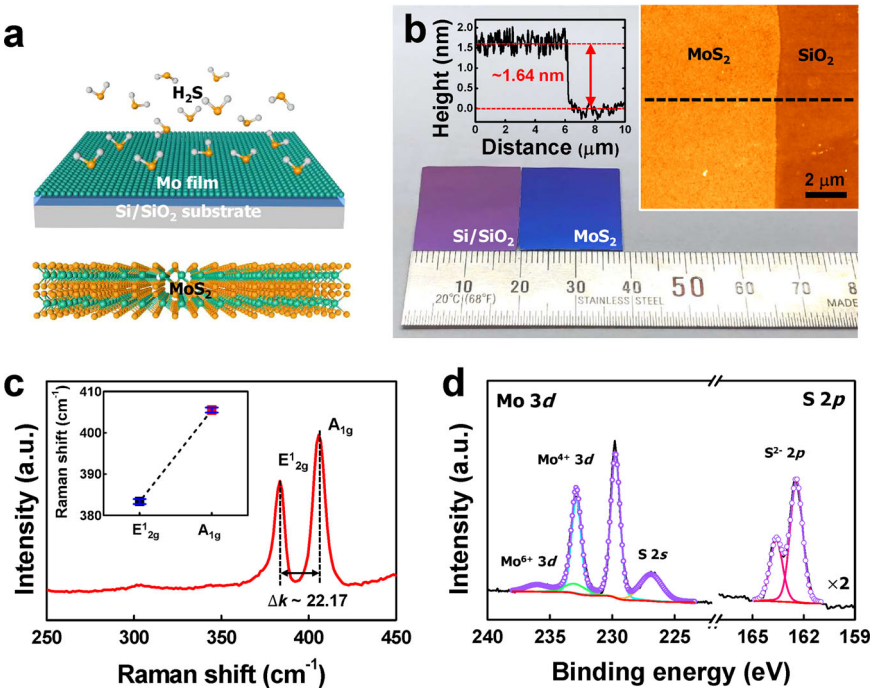

Fig. 1 MoS_2 synthesized by two-step method. a Schematic image of two-step growth of bilayer MoS_2. **b** Optical image of MoS_2 film and Si/SiO_2 substrate, and thickness profile of MoS_2 film. **c** Raman and **d** XPS spectra of MoS_2 films.

determines the thickness of the final MoS_2 film, is controlled by the sputtering parameters and the deposition time[41]. However, in case of thick Mo film (>5 nm), it could not be completely sulfurized due to the limited diffusion length of sulfur (S) atoms, resulting in multiphase film with MoS_2 on top and Mo underneath[41,42]. To obtain fully sulfurized MoS_2 films, we deposited ultra-thin Mo film with the thickness of 2 nm by optimizing the deposition time to 180 s. In the optical image of Fig. 1b, the fabricated MoS_2 film showed a blue color, which is completely different from the purple color of Si/SiO_2 substrate, with a highly uniform distribution over a centimeter scale, denoting its continuity and connectivity of the large-area MoS_2 film. The thickness of the MoS_2 film was measured as 1.64 nm using atomic force microscopy (AFM), which may suggest two MoS_2 layers (insets of Fig. 1b). Raman spectrum of the MoS_2 film (Fig. 1c) showed two typical peaks of in-plane (E^1_{2g}) and out-of-plane (A_{1g}) modes at 383.52 cm^{-1} and 405.69 cm^{-1}, respectively. The peak difference (Δk) between the E^1_{2g} and A_{1g} modes was calculated to be 22.17 cm^{-1}, corresponding to bilayer MoS_2[43], consistently with the AFM result. The average values of the E^1_{2g} and A_{1g} peaks from randomly distributed nine points on the 2×2 cm^2 MoS_2 film were estimated to 383.32 and 405.49 cm^{-1}, respectively, with Δk of 22.17 cm^{-1} (Inset of Fig. 1c), indicating high homogeneity of bilayer MoS_2 on large-area.

X-ray photoelectron spectroscopy (XPS) was employed to identify chemical binding states of Mo and S atoms in the MoS_2 film. XPS spectra of Mo 3*d* and S 2*p* core levels of the MoS_2 film including deconvolution curves were depicted in Fig. 1d. In Mo 3*d* spectrum, two strong doublet peaks were observed at 229.75 (Mo^{4+} $3d_{5/2}$) and 232.88 eV (Mo^{4+} $3d_{3/2}$), respectively, corresponding to MoS_2 bonding[44]. In addition, two small doublets peaks of Mo^{6+} $3d_{5/2}$ and Mo^{6+} $3d_{3/2}$ were confirmed at 232.93 and 236.06 eV, respectively, which were attributed to the existence of residual MoO_3[44]. However, the atomic fractions of the Mo^{6+}, which was estimated to be 13% (<20% of the total Mo species), is reasonable for air-exposed MoS_2 films[45]. In the S 2*p* spectrum, only two doublet peaks belonging to MoS_2 bonding appeared at 162.44 (S^{2-} $2p_{3/2}$) and 163.62 eV (S^{2-} $2p_{1/2}$), respectively. The quantitative ratio between S^{2-} 2*p* and Mo^{4+} 3*d* was ~1.96, which indicates a perfect MoS_2 configuration.

Transmission electron microscopy observations of MoS_2 film. The atomic structure of the MoS_2 film was explored through transmission electron microscopy (TEM). The cross-sectional TEM image of the MoS_2 film shows its 2D bilayer structure as shown in Fig. 2a. A plan-view TEM image of the MoS_2 over an area of 41×41 nm^2 exhibits its large-area continuous lattice (Fig. 2b). In addition, several kinds of Moirè patterns were observed, indicating a lattice mismatch between two layers. A layered structure is formed by the van der Waals (vdW) interactions between the different layers. The relatively weak vdW forces can induce variations in strain response between adjacent layers, resulting in the lattice mismatch by sliding the layer or nucleating ripples[46]. The MoS_2 films with Moirè fringes exhibit a ring-shape of fast Fourier transform (FFT) pattern (Inset of Fig. 2b), suggesting a polycrystalline structure of the films. The high-resolution TEM image of Fig. 2c shows partially well-organized hexagonal lattice structures along with grain boundaries. In Fig. 2d, two MoS_2 grains of (100) plane meet each other with a relative misorientation of 30°, and the corresponding FFT patterns of the high-resolution TEM image (Inset of Fig. 2d) reveal their diffraction spots indicated with different colors. Despite the insufficient statistical data to identify the size of the MoS_2 grain, we can anticipate that many grain boundaries were possessed in the polycrystalline MoS_2 films.

Electrical properties of MoS_2 TFTs. To investigate electrical characteristics of the large-area synthesized MoS_2 films, we fabricated MoS_2 TFTs as shown in Fig. 3a. The MoS_2 films on Si/SiO_2 substrate were patterned by photolithography combined with dry etching to obtain active channels for transistors. Titanium (Ti) and gold (Au) electrodes were placed for source and drain contacts. Figure 3b illustrates bottom gate voltage (V_{GS})–drain current (I_{DS}) curves of the MoS_2 TFT in logarithmic (red circle line) and linear (blue square line) scales with V_{GS} range from –40 to 40 V and drain voltage (V_{DS}) of 1 V, where a channel width (W) and length (L) were 20 and 7 μm, respectively. We observed an excellent n-type semiconducting property with a very high on–off ratio (I_{on}/I_{off}) over 2×10^6. V_{DS}–I_{DS} curves of the MoS_2 TFT obtained in the V_{GS} range from –40 to 40 V at intervals of 10 V (Fig. 3c) also exhibited typical n-type characteristics. Here, the top–down approach of the sputtered MoS_2 facilitated a large-volume integrated 2D MoS_2 sensor arrays on a substrate. Figure 3d shows statistics on the electrical parameters of maximum transconductance (g_m) and V_{TH} obtained by randomly distributed 24 MoS_2 TFTs on a substrate (Supplementary Fig. 1), revealing very narrow distributions and small standard deviations of 9% for g_m and 17% for V_{TH}, respectively. These statistical distribution of as-fabricated transistors shows superior electrical uniformity.

NO_2 gas-sensing behavior. NO_2 gas not only has a huge impact on the environment but can also be a diagnostic tool for breath analysis[47]. To confirm sensing responses of the MoS_2 TFT to NO_2 gas, the device was mounted on a stage in a gas chamber equipped with a semiconductor characterization system. An optical image of the MoS_2 gas-sensing TFT was shown in Fig. 4a, where W/L of the device was 20/7 μm. Figure 4b shows V_{GS}–I_{DS} curves of the MoS_2 gas sensor measured under various concentrations of NO_2 gas from 0 to 256 ppm. Increasing the NO_2 concentration resulted in the significant decrease of I_{DS} over the whole range of V_{GS}, which denotes that the NO_2 adsorption on the MoS_2 surface reduces the conductivity of the MoS_2 channel. We also measured a time-resolved sensing response of the device to confirm its real-time current behavior when NO_2 gas was injected into the chamber for 5 min, and then the sensor was recovered via pure N_2 purging for 5 min (Fig. 4c). The concentration of NO_2 gas was ranged from 8 to 256 ppm, and 1 V of V_{DS} was applied. The response is calculated as $(R_{gas}-R_0)/R_0$, where R_{gas} represents a resistance of the device under the NO_2 gas environment and R_0 is its initial resistance without NO_2 gas exposure. V_{GS} was fixed at 0 V since most MoS_2 TFTs exhibited higher response values at V_{GS} near 0 V (Supplementary Figs. 2a–d). Considering that the average V_{TH} of the MoS_2 TFTs was evaluated as 13.5 V (Fig. 3d), V_{GS} range near 0 V is considered as a subthreshold regime. The high response in subthreshold region has been proposed earlier in many TFT-based sensors[48–50]. In Fig. 4c, as the NO_2 concentration increased, R_{gas} also increased, resulting in positive values of response. However, the response value was not saturated within 5 min owing to a continuous condensation of gas molecules on the MoS_2 surface[51,52]. When we measured the electrical response longer than 5 min (Supplementary Fig. 3), the saturation in sensing response was observed. In addition, rapid recovery was observed when the NO_2 gas was removed (Fig. 4c), indicating great suitability of MoS_2 TFTs for gas-sensing applications. To confirm a limit of detection of the MoS_2 gas sensor, we tried to measure the sensing response of the device at lower ppm level from 1 to 4 ppm. The sensor presented the response value of 0.5% for 1 ppm of NO_2 concentration (Supplementary Fig. 4).

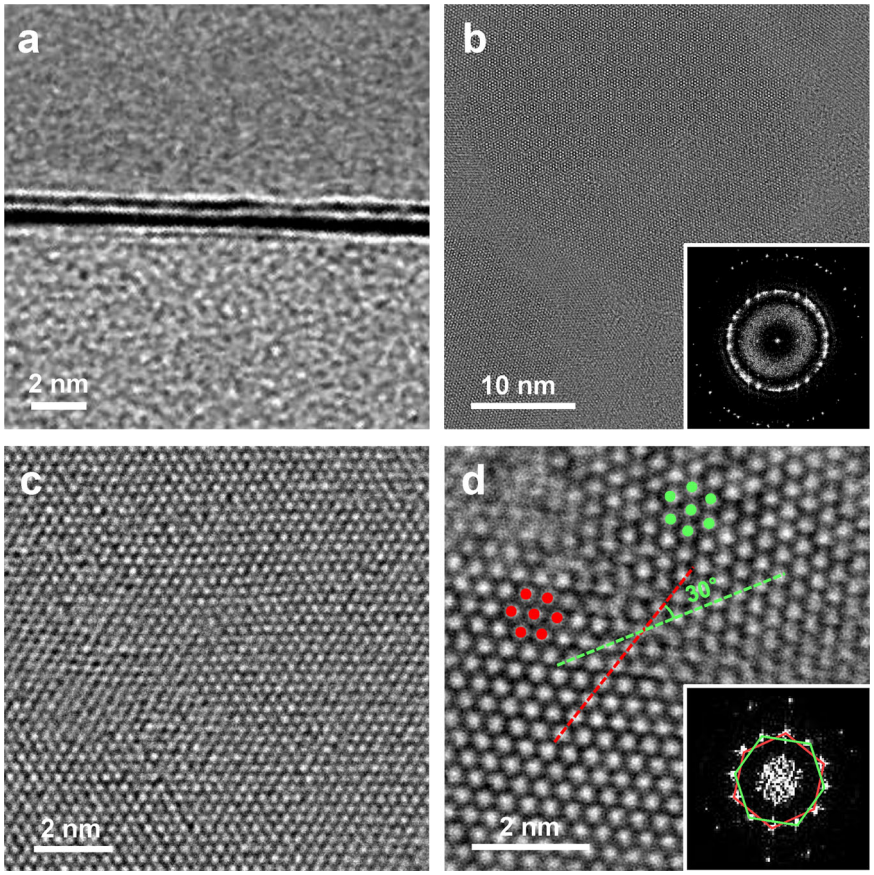

Fig. 2 TEM images of MoS_2 film. a Cross-sectional and **b** plan-view TEM images. **c** Basal plane and **d** grain boundary (Inset of FFT patterns extracted from each figure).

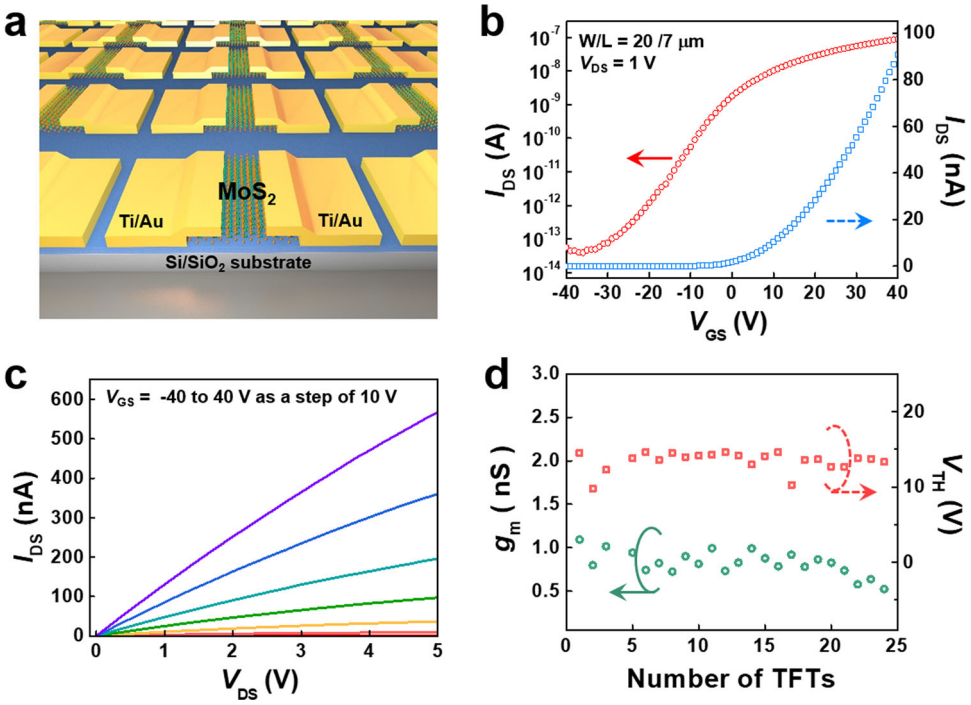

Fig. 3 Electrical properties of MoS_2 TFTs. a Schematic image of MoS_2 TFTs. **b** Transfer characteristics and **c** output characteristics of MoS_2 TFT. **d** Plot of g_m and V_{TH} of 24 different MoS_2 TFTs.

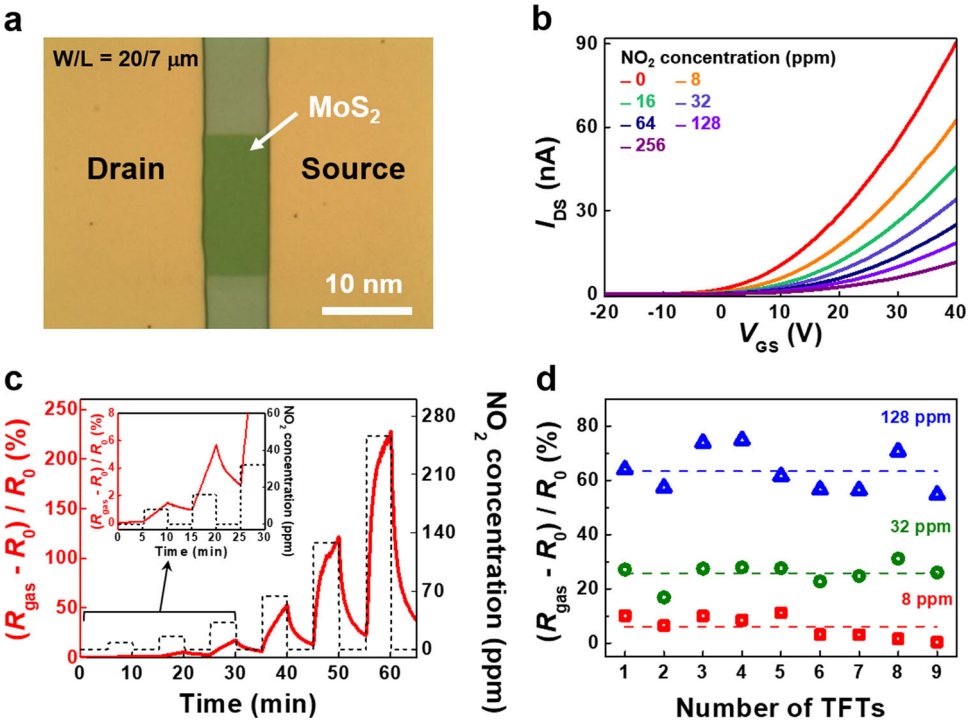

Fig. 4 NO_2 gas-sensing performances of MoS_2 TFTs. a Optical microscopic image of MoS_2 TFT. **b** Transfer characteristics of MoS_2 TFT upon NO_2 exposure with different concentrations ranging from 0 to 256 ppm. **c** Real-time sensing response of gas sensor with NO_2 exposure from 8 to 256 ppm concentration. **d** Response of nine different gas sensors measured at NO_2 concentrations of 8, 32, and 128 ppm and average response at each concentration.

To evaluate a sensing uniformity of the MoS_2 gas sensors, the sensing responses of nine different devices were examined under the injection of various NO_2 concentrations. The response of each TFT was presented by different colors depending on different concentrations of NO_2; red for 8 ppm, green for 32 ppm and blue for 128 ppm, and the average values of nine TFTs were marked as dotted lines. The response of each device did not deviate significantly from the mean value, which was supported by low standard errors of 1.36, 1.34, and 2.65, respectively.

For in-depth study of the sensing mechanism of the two-step-grown MoS_2 gas sensor, we examined variations of device electrical parameters of the device under increasing NO_2 gas concentrations. The V_{TH} and μ_{FE} values were extracted from each V_{GS}–I_{DS} curves in Fig. 4b. In Fig. 5a, the variation of V_{TH} (ΔV_{TH}) is plotted as a function of NO_2 concentration, indicating continuous positive shift of V_{TH}, especially, with rapid changes in low concentrations. Moreover, μ_{FE} gradually degraded when the NO_2 concentrations increased (blue circle in Fig. 5b). These electrical behaviors are unequivocally different from the previously reported exfoliated MoS_2 TFT gas sensors[29,53]. As shown in Supplementary Fig. 5a, for comparison purposes, we also measured the sensing responses of exfoliated MoS_2 TFT having a channel area similar to that of the two-step-grown MoS_2 TFT. In the exfoliated MoS_2 gas sensors, NO_2 gas molecules are physically adsorbed on the basal surface of the MoS_2 by vdW interactions[32,54–56], which generates in-gap states in bandgap region close to the valence band and thus, increases the tunneling of hole carriers[29,53]. As a result, I_{off} for the transistor gradually increased along with NO_2 concentrations (Supplementary Fig. 5b). However, these devices showed no change in μ_{FE} according to NO_2 concentrations, as shown in an orange square in Fig. 5b, unlike the two-step-grown MoS_2 TFT. The major difference between two MoS_2 FETs is the crystalline structure of MoS_2 films, i.e., the two-step-grown MoS_2 film is polycrystalline, whereas the exfoliated MoS_2 flake is single-crystal. On the polycrystalline MoS_2 surface, the abundant grain boundaries are expected to serve as active binding sites for NO_2 molecules, so that the adsorption of NO_2 on grain boundaries is more dominant than that on basal plane[57–59], as shown in schematic illumination of an inset of Fig. 5a. This can be further understood by the fact that the shifts of V_{TH} and μ_{FE} variation were gradually diminished as the grain boundaries became saturated.

There are many reports on organic TFT-based chemical sensors, having many grain boundaries in their channels, like the two-step-grown MoS_2[59–61]. In organic TFT sensors, the adsorption of gas analytes on the grain boundaries induces local electric fields through polarization of the semiconductor, leading to the trapping of mobile carriers, and consequently, to variations in current behaviors. To establish the relationship between the NO_2 adsorption on the MoS_2 grain boundaries and the I_{DS} decrease involving the variations of V_{TH} and μ_{FE}, the temperature-dependent current behavior measurements were conducted on two-step-grown MoS_2 TFT with and without NO_2 gas exposure. We measured V_{GS}–I_{DS} curves at different temperatures from 350 to 400 K at intervals of 10 K under pure N_2 (Supplementary Fig. 6a) and NO_2 environments with the concentration of 256 ppm (Supplementary Fig. 6b). In both cases, two devices exhibited thermally activated I_{DS} when the temperature increased. We extracted a carrier activation energy (E_A) from experimentally measured results by using the following equation:

$$I_{DS} = I_{D0} exp(-E_A/k_B T)$$

where I_{D0} is the prefactor, k_B is the Boltzmann constant, and T is temperature[62–64]. Supplementary Figs. 7a and b plot I_{DS} as a function of $1/k_B T$ derived from Supplementary Figs. 6a and b,

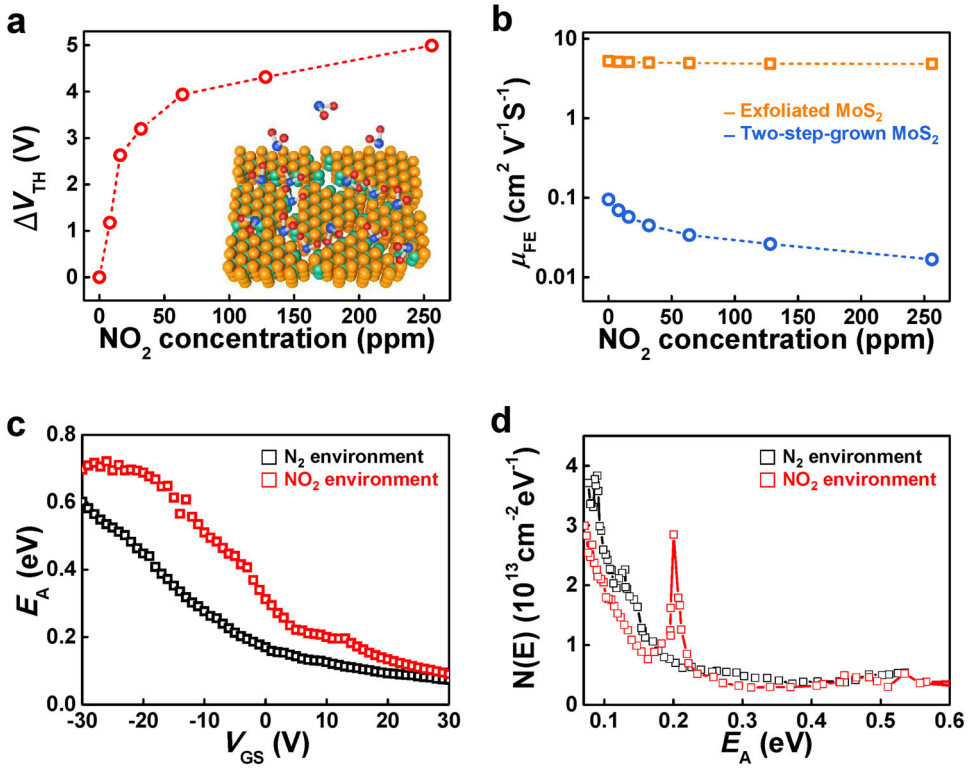

Fig. 5 Atomic structure-dependent NO_2 sensing behavior. a ΔV_{TH} according to NO_2 exposure and schematic image of NO_2 adsorption on MoS_2 grain boundaries (inset). **b** Comparison of μ_{FE} between exfoliated and two-step-grown MoS_2 TFTs under different concentrations of NO_2. **c** Calculated activation energy (E_A) as a function of V_{GS} and **d** density of states for MoS_2 TFT with and without NO_2 gas exposure.

respectively, and Supplementary Figs. 7c and d are I_{D0} according to V_{GS}. The calculated E_A curves according to V_{GS} are presented in Fig. 5c, which show a higher E_A values under NO_2 environment than only N_2 environment in the whole range of V_{GS}. This indicates that the absorption of NO_2 gas molecules induced a higher potential barrier for electron carriers to hop to the next grain. Furthermore, we can estimate the density of sub-gap states as follows:

$$N(E) = C_{ox}q^{-1}\left(\partial E_A \partial V_{GS}^{-1}\right)^{-1}$$

where C_{ox} is oxide capacitance and q is electron charge. Figure 5d shows the calculated density of states near conduction band (E_c). A new sub-state was observed near E_c–0.2 eV under NO_2 environment, providing direct evidence of the formation of trap state. These results indicate that the NO_2 adsorption on the grain boundaries generates trap states in the forbidden band, inducing charge trapping and increment in the potential barrier, which inhibits the carrier transport in the channel and induces the decrease of I_{DS} and μ_{FE}.

Active-matrix of gas sensors based on MoS_2 TFT. Large-area and uniform MoS_2 films enable to manufacture a monolithically integrated circuit of active-matrix gas sensor array. Figure 6a shows an optical image of the NO_2 gas-sensing active-matrix consisting of 7×6 pixels; each pixel contains both one switching TFT and one sensing TFT based on large-area synthesized MoS_2 film as shown in Fig. 6b. Switching TFTs were operated by local bottom gate separated from back gate and an 80 nm thick aluminum oxide (Al_2O_3) was used as gate dielectric. To prevent the reaction between NO_2 gas molecules and MoS_2 of switching transistors, their MoS_2 channels were encapsulated by a 20 nm thick SiO_2 insulator. Figure 6c shows the transfer curve of a switching MoS_2 TFT at a supplied voltage (V_{DD}) of 1 V under switching gate bias (V_{SW}) from −10 to 10 V. The switching states of the MoS_2 TFT were determined to be ON when V_{SW} is 10 V and OFF when V_{SW} is −10 V, respectively. Based on the electrical property of the switching TFT, we operated the integrated gas-sensing circuit under different NO_2 gas concentrations from 8 to 64 ppm at V_{DD} of 1 V (Fig. 6d). Here, back gate voltage (V_{Back}) was fixed at 0 V so that the sensing TFTs can operate in subthreshold regime. V_{SW} was applied to 10 and −10 V periodically for 5 min. When the device is on the ON state (V_{SW} of 10 V), the channel of switching TFT was opened and the drain current flowed through the channel of sensing TFT. Under NO_2 environment, the device current (I_{DD}) gradually decreased in a good agreement with the sensing behavior of the single MoS_2 TFT as shown in Fig. 4c. However, the OFF state (V_{SW} of −10 V) limits the current flow in the channel of sensing TFT, resulting in current values independent of NO_2 concentrations. As a result, both the great sensing and switching performances of the two-step-grown MoS_2 gas sensor active-matrix were confirmed in Fig. 6d. In addition, statistical distributions of the switching and gas-sensing properties of active matrix were presented in the mapping images that present the I_{DD} level of each MoS_2 pixel before and after the exposure of NO_2 gas when the devices were on the OFF (Supplementary Fig. 8a) and ON (Supplementary Fig. 8b) states, respectively. V_{DD} of 1 V and V_{Back} of 0 V were fixed, respectively. All 42 MoS_2 gas sensors exhibited no noticeable variation in I_{DD} values when the devices were OFF state. However, at ON state, the I_{DD} values of all gas sensors were reduced when the NO_2 gas was added. However, the differences in the electrical properties were existed for each pixel. Therefore, device calibration is required for practical use.

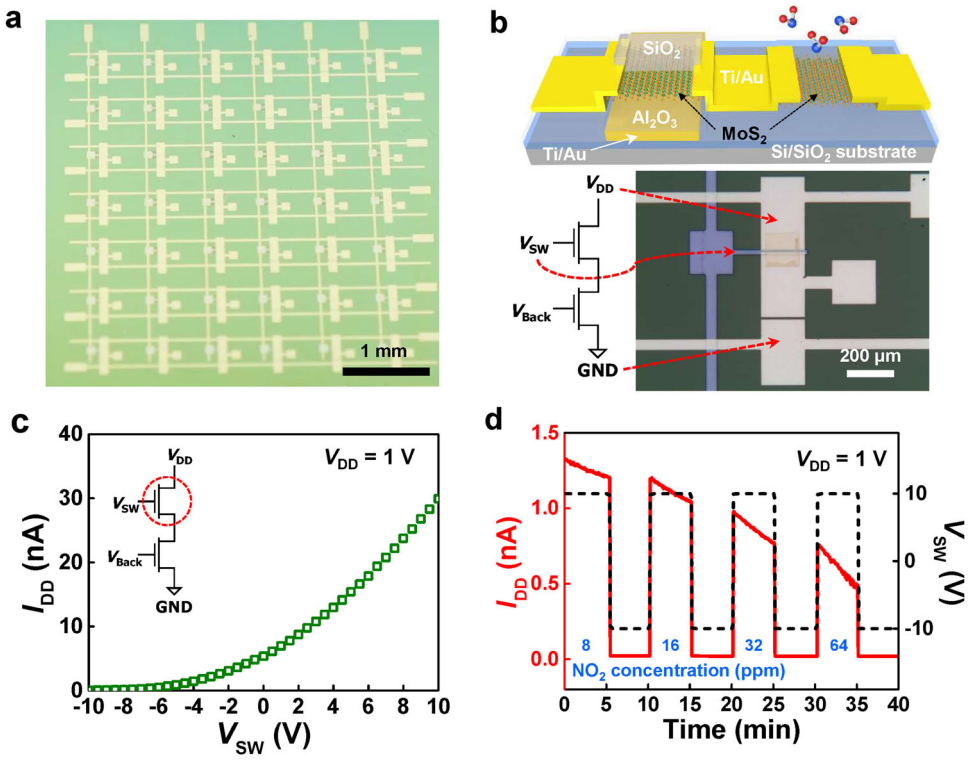

Fig. 6 MoS_2 TFTs-based gas sensor active-matrix. a Image of MoS_2 gas sensor active-matrix consisting of 7 × 6 pixels. **b** Schematic image, circuit diagram, and optical image of integrated single pixel containing a switching TFT and a sensing TFT. **c** Transfer characteristic of switching TFT. **d** NO_2 gas-sensing behavior of MoS_2 gas sensor active device under dynamic switching.

Conclusion

In summary, we have demonstrated active-matrix gas sensor array with pixel circuits comprising gas-sensing TFT and switching TFT based on two-step-grown large-area MoS_2 films. Consistent g_m as well as I_{on}/I_{off} ratio of ~ 2×10^6 were obtained across a few centimeters of the grown film. The MoS_2 TFT-based gas sensors can detect as low as 1 ppm of NO_2 level with a wide detection range of up to 256 ppm, and the decent gas-sensing performance are attributed to the abundant grain boundaries of the sputtered polycrystalline MoS_2 channel as investigated via structural TEM analysis as well as temperature-dependent current measurements with corresponding sub-gap states analysis. Furthermore, the pixel circuit of the demonstrated 7 × 6 active-matrix gas sensor array is capable of NO_2 gas sensing as well as electrical switching depending on operation regimes. The proposed two-step-grown MoS_2 TFT-based gas sensors with highly sensitive detection of gas molecules and scalability into integrated systems have enormous potential as a standard gas-sensing platform.

Methods

MoS_2 growth. Mo was deposited on P-type boron-doped Si/SiO_2 (300 nm) substrates, which were preliminarily cleaned in an ultrasonic bath for 10 min by sequentially using acetone, isopropyl alcohol, and deionized water. Both a Mo target (99.99%) with a 101.6 mm diameter and these substrates were placed in the sputtering chamber under high-vacuum conditions (<3×10^{-6} Torr). The working pressure was maintained at 10 mTorr with an Ar flow of 100 sccm. Prior to the deposition, the Mo target was pre-sputtered for 10 min to remove its oxidized surface and enhance the plasma stability. The Mo deposition was conducted with RF power of 150 W for 180 s at room temperature. The as-deposited Mo films were then placed in a CVD chamber for the sulfurization. The chamber temperature was raised to 750 °C for 30 min. Only Ar gas (50 sccm) was injected until 300 °C. At the higher temperatures, Ar/H_2/H_2S (50:5:1) gas mixture was added for 15 min. After the sulfurization process, the high temperature of 950 °C was maintained for 1 h to improve the crystallinity of synthesized MoS_2 films.

Characterizations. The thickness of MoS_2 film was measured with AFM (XE7 Atomic Force Microscope, Park Systems). Raman spectra was obtained by Micro-Raman spectrometer system (ALPHA300, WITec Co.) at the MEMS · Sensor Platform Center of Sungkyunkwan University (SKKU) with an excitation laser at 532 nm with a power of 0.5 mW. XPS analysis was also conducted using AR-XPS system (Theta Probe AR-XPS System, ThermoFisher Scientific) with monochromated Al *Ka* radiation (1486.6 eV). For TEM measurments, the MoS_2 film was transferred onto copper (Cu) grids with a lacey carbon support film. Cross-sectional and plan-view TEM images were obtained by aberration corrected TEM(JEM-ARM200F, JEOL Ltd.) with an accelerating voltage of 80 kV. The electrical properties of the MoS_2 TFTs were investigated using a semiconductor characterization system (Keithley 4200 SCS, Keithley) and dark box under ambient condition.

Fabrications of MoS_2 TFT. The synthesized MoS_2 films were patterned via photolithography using mask aligner (MA6, SUSS MicroTec) and oxygen plasma reactive ion etching at 30 sccm and 50 W for 1 min to obtain TFT channels. For the lift-off process, the source and drain were pre-patterned through photolithography and, then, Ti/Au (20 nm/100 nm) were deposited by an electron beam evaporator. After the removal of the unnecessary Ti/Au part, the samples were annealed at 200 °C for 2 h in a vacuum chamber to improve the electrical junctions.

NO_2 gas-sensing measurement. The fabricated MoS_2 FET-based gas sensors were inserted in a sensing chamber designed to evaluate the electrical properties under a gas flow. Before the gas injection, the vacuum condition (10 mTorr) was applied to remove unnecessary gases. NO_2 gas was diluted with N_2 gas; the flow rate of the injected gases was controlled by mass flow controllers and the total flow rate was maintained at 1000 sccm for the whole time. Before measuring the electrical properties of the sensors, each sample device was exposed to NO_2 gas for 10 min at room temperature.

Data availability

The data supporting the findings of this study are included in this paper and its supplementary information.

Received: 18 April 2020; Accepted: 8 September 2020;
Published online: 13 November 2020

References

1. Zhang, J., Liu, X., Neri, G. & Pinna, N. Nanostructured materials for room-temperature gas sensors. *Adv. Mater.* **28**, 795–831 (2016).
2. Andringa, A. M., Piliego, C., Katsouras, I., Blom, P. W. M. & de Leeuw, D. M. NO_2 detection and real-time sensing with field-effect transistors. *Chem. Mater.* **26**, 773–785 (2014).
3. Liu, X. et al. A survey on gas sensing technology. *Sensors* **12**, 9635–9665 (2012).
4. Billi, E., Viricelle, J. P., Montanaro, L. & Pijolat, C. Development of a protected gas sensor for exhaust automotive applications. *IEEE Sens. J.* **2**, 342–348 (2002).
5. Di Natale, C., Paolesse, R., Martinelli, E. & Capuano, R. Solid-state gas sensors for breath analysis: a review. *Anal. Chim. Acta* **824**, 1–17 (2014).
6. Barsan, N., Koziej, D. & Weimar, U. Metal oxide-based gas sensor research: how to? *Sens. Actuat. B Chem.* **121**, 18–35 (2007).
7. Franke, M. E., Koplin, T. J. & Simon, U. Metal and metal oxide nanoparticles in chemiresistors: does the nanoscale matter? *Small* **2**, 36–50 (2006).
8. McCue, J. T. & Ying, J. Y. SnO_2-In_2O_3 nanocomposites as semiconductor gas sensors for CO and NO_x detection. *Chem. Mater.* **19**, 1009–1015 (2007).
9. Kim, I. D. et al. Ultrasensitive chemiresistors based on electrospun TiO_2 nanofibers. *Nano Lett.* **6**, 2009–2013 (2006).
10. Barsan, N. & Weimar, U. Conduction model of metal oxide gas sensors. *J. Electroceram.* **7**, 143–167 (2001).
11. Sun, Y. F. et al. Metal oxide nanostructures and their gas sensing properties: a review. *Sensors* **12**, 2610–2631 (2012).
12. McAlpine, M. C., Ahmad, H., Wang, D. W. & Heath, J. R. Highly ordered nanowire arrays on plastic substrates for ultrasensitive flexible chemical sensors. *Nat. Mater.* **6**, 379–384 (2007).
13. Fahad, H. M. et al. Room temperature multiplexed gas sensing using chemical-sensitive 3.5-nm-thin silicon transistors. *Sci. Adv.* **3**, 8 (2017).
14. Torsi, L., Dodabalapur, A., Sabbatini, L. & Zambonin, P. G. Multi-parameter gas sensors based on organic thin-film-transistors. *Sens. Actuat. B Chem.* **67**, 312–316 (2000).
15. Zhang, J., Boyd, A., Tselev, A., Paranjape, M. & Barbara, P. Mechanism of NO_2 detection in carbon nanotube field effect transistor chemical sensors. *Appl. Phys. Lett.* **88**, 3 (2006).
16. Cui, Y., Wei, Q. Q., Park, H. K. & Lieber, C. M. Nanowire nanosensors for highly sensitive and selective detection of biological and chemical species. *Science* **293**, 1289–1292 (2001).
17. Han, J. W., Rim, T., Baek, C. K. & Meyyappan, M. Chemical gated field effect transistor by hybrid integration of one-dimensional silicon nanowire and two-dimensional tin oxide thin film for low power gas sensor. *ACS Appl. Mater. Interfaces* **7**, 21263–21269 (2015).
18. Shehada, N. et al. Ultrasensitive silicon nanowire for real-world gas sensing: noninvasive diagnosis of cancer from breath volatolome. *Nano Lett.* **15**, 1288–1295 (2015).
19. Kong, J. et al. Nanotube molecular wires as chemical sensors. *Science* **287**, 622–625 (2000).
20. Mirica, K. A., Azzarelli, J. M., Weis, J. G., Schnorr, J. M. & Swager, T. M. Rapid prototyping of carbon-based chemiresistive gas sensors on paper. *Proc. Natl. Acad. Sci. USA* **110**, E3265–E3270 (2013).
21. Li, J., Lu, Y. J., Ye, Q., Delzeit, L. & Meyyappan, M. A gas sensor array using carbon nanotubes and microfabrication technology. *Electrochem. Solid State Lett.* **8**, H100–H102 (2005).
22. Gao, T., Woodka, M. D., Brunschwig, B. S. & Lewis, N. S. Chemiresistors for array-based vapor sensing using composites of carbon black with low volatility organic molecules. *Chem. Mater.* **18**, 5193–5202 (2006).
23. Janata, J. & Josowicz, M. Organic semiconductors in potentiometric gas sensors. *J. Solid State Electrochem.* **13**, 41–49 (2009).
24. Zang, Y. P. et al. Specific and reproducible gas sensors utilizing gas-phase chemical reaction on organic transistors. *Adv. Mater.* **26**, 2862–2867 (2014).
25. Schedin, F. et al. Detection of individual gas molecules adsorbed on graphene. *Nat. Mater.* **6**, 652–655 (2007).
26. Cui, S. M. et al. Ultrahigh sensitivity and layer-dependent sensing performance of phosphorene-based gas sensors. *Nat. Commun.* **6**, 9 (2015).
27. Donarelli, M. & Ottaviano, L. 2D materials for gas sensing applications: a review on graphene oxide, MoS_2, WS_2 and phosphorene. *Sensors* **18**, 45 (2018).
28. Liu, X. H., Ma, T. T., Pinna, N. & Zhang, J. Two-dimensional nanostructured materials for gas sensing. *Adv. Funct. Mater.* **27**, 30 (2017).
29. Baek, J. et al. A highly sensitive chemical gas detecting transistor based on highly crystalline CVD-grown $MoSe_2$ films. *Nano Res.* **10**, 1861–1871 (2017).
30. Li, H. et al. Fabrication of single- and multilayer MoS_2 film-based field-effect transistors for sensing NO at room temperature. *Small* **8**, 63–67 (2012).
31. Donarelli, M. et al. Response to NO_2 and other gases of resistive chemically exfoliated MoS_2-based gas sensors. *Sens. Actuat. B Chem.* **207**, 602–613 (2015).
32. Late, D. J. et al. Sensing behavior of atomically thin-layered MoS_2 transistors. *ACS Nano* **7**, 4879–4891 (2013).
33. Tao, L. et al. Centimeter-scale CVD growth of highly crystalline single-layer MoS_2 film with spatial homogeneity and the visualization of grain boundaries. *ACS Appl. Mater. Interfaces* **9**, 12073–12081 (2017).
34. Yu, Y. F. et al. Controlled scalable synthesis of uniform, high-quality monolayer and few-layer MoS_2 films. *Sci Rep.* **3**, 6 (2013).
35. Pyeon, J. J. et al. Wafer-scale growth of MoS_2 thin films by atomic layer deposition. *Nanoscale* **8**, 10792–10798 (2016).
36. Kang, K. et al. High-mobility three-atom-thick semiconducting films with wafer-scale homogeneity. *Nature* **520**, 656–660 (2015).
37. Huang, J. H. et al. Large-area few-layer MoS_2 deposited by sputtering. *Mater. Res. Express* **3**, 7 (2016).
38. Park, H. et al. Exceptionally uniform and scalable multilayer MoS_2 phototransistor array based on large-scale MoS_2 grown by RF sputtering, electron beam irradiation, and sulfurization. *ACS Appl. Mater. Interfaces* **12**, 20645–20652 (2020).
39. Muratore, C. et al. Continuous ultra-thin MoS_2 films grown by low-temperature physical vapor deposition. *Appl. Phys. Lett.* **104**, 5 (2014).
40. Hussain, S. et al. Large-area, continuous and high electrical performances of bilayer to few layers MoS_2 fabricated by RF sputtering via post-deposition annealing method. *Sci. Rep.* **6**, 13 (2016).
41. Jo, S. S. et al. Formation of large-area MoS_2 thin films by oxygen-catalyzed sulfurization of Mo thin films. *J. Vac. Sci. Technol. A* **38**, 013405 (2020).
42. Park, J. et al. Thickness modulated MoS_2 grown by chemical vapor deposition for transparent and flexible electronic devices. *Appl. Phys. Lett.* **106**, 5 (2015).
43. Li, H. et al. From bulk to monolayer MoS_2: evolution of raman scattering. *Adv. Funct. Mater.* **22**, 1385–1390 (2012).
44. Brown, N. M. D., Cui, N. Y. & McKinley, A. An XPS study of the surface modification of natural MoS_2 following treatment in an RF-oxygen plasma. *Appl. Surf. Sci.* **134**, 11–21 (1998).
45. Ko, T. Y. et al. On-stack two-dimensional conversion of MoS_2 into MoO_3. *2D Mater* **4**, 12 (2017).
46. Wang, J., Namburu, R., Dubey, M. & Dongare, A. M. Origins of moire patterns in CVD-grown MoS_2 bilayer structures at the atomic scales. *Sci. Rep.* **8**, 9 (2018).
47. Zhou, Y., Gao, C. & Guo, Y. UV assisted ultrasensitive trace NO_2 gas sensing based on few-layer MoS_2 nanosheet–ZnO nanowire heterojunctions at room temperature. *J. Mater. Chem. A* **6**, 10286–10296 (2018).
48. Sarkar, D. & Banerjee, K. Proposal for tunnel-field-effect-transistor as ultra-sensitive and label-free biosensors. *Appl. Phys. Lett.* **100**, 143108 (2012).
49. Gao, X. P. A., Zheng, G. & Lieber, C. M. Subthreshold regime has the optimal sensitivity for nanowire FET biosensors. *Nano Lett.* **10**, 547–552 (2009).
50. Sarkar, D. et al. MoS_2 field-effect transistor for next-generation label-free biosensors. *ACS Nano* **8**, 3992–4003 (2014).
51. He, Q. et al. Fabrication of flexible MoS_2 thin-film transistor arrays for practical cas-sensing applications. *Small* **8**, 2994–2999 (2012).
52. Robinson, J. A. et al. Role of defects in single-walled carbon nanotube chemical sensors. *Nano Lett.* **6**, 1747–1751 (2006).
53. Im, H. et al. On MoS_2 thin-film transistor design consideration for a NO_2 gas sensor. *ACS Sens.* **4**, 2930–2936 (2019).
54. Li, W. L. et al. Gas sensors based on mechanically exfoliated MoS_2 nanosheets for room-temperature NO_2 detection. *Sensors* **19**, 12 (2019).
55. Perkins, F. K. et al. Chemical vapor sensing with monolayer MoS_2. *Nano Lett.* **13**, 668–673 (2013).
56. Yue, Q., Shao, Z. Z., Chang, S. L. & Li, J. B. Adsorption of gas molecules on monolayer MoS_2 and effect of applied electric field. *Nanoscale Res. Lett.* **8**, 7 (2013).
57. Torsi, L. et al. Regioregular polythiophene field-effect transistors employed as chemical sensors. *Sens. Actuat. B Chem.* **93**, 257–262 (2003).
58. Wang, L., Fine, D., Khondaker, S. I., Jung, T. & Dodabalapur, A. Sub 10 nm conjugated polymer transistors for chemical sensing. *Sens. Actuat. B Chem.* **113**, 539–544 (2006).
59. Duarte, D. & Dodabalapur, A. Investigation of the physics of sensing in organic field effect transistor based sensors. *J. Appl. Phys.* **111**, 7 (2012).
60. Wang, L., Fine, D. & Dodabalapur, A. Nanoscale chemical sensor based on organic thin-film transistors. *Appl. Phys. Lett.* **85**, 6386–6388 (2004).
61. Kim, S. & Dodabalapur, A. Polarization effects from the ambient and the gate dielectric on charge transport in polymer field-effect transistors. *Appl. Phys. Lett.* **110**, 4 (2017).
62. Chen, C., Abe, K., Kumomi, H. & Kanicki, J. Density of states of a-InGaZnO from temperature-dependent field-effect studies. *IEEE Trans. Electron. Devices* **56**, 1177–1183 (2009).
63. Horowitz, G., Hajlaoui, M. E. & Hajlaoui, R. Temperature and gate voltage dependence of hole mobility in polycrystalline oligothiophene thin film transistors. *J. Appl. Phys.* **87**, 4456–4463 (2000).
64. Jung, C. et al. Highly crystalline CVD-grown multilayer $MoSe_2$ thin film transistor for fast photodetector. *Sci. Rep.* **5**, 9 (2015).

Acknowledgements

This research was supported in part by the National Research Foundation of Korea (2018R1A2B2003558 and 2015R1A5A1037548). This work was supported in part by the Industrial Strategic Technology Development Program (20000300) funded by the Ministry of Trade, Industry and Energy (MOTIE, Korea) and the Korea Basic Science Institute(KBSI) National Research Facilities & Equipment Center(NFEC) grant funded by the Korea government (Ministry of Education) (no. 2019R1A6C1010031).

Author contributions

Sunkook Kim and G. Yoo conceived the project. Sehwan Kim and H. Park, and J.Y. Yang fabricated the TFT-based gas sensor using the MoS_2 synthesized by S. Choo and S. Baek. Y. Kwon, N. Liu, and C.-W. Yang contributed to structural and chemical characterizations of the MoS_2 using TEM and XPS. All authors wrote and contributed to the manuscript.

Competing interests

The authors declare no competing financial or non-financial interests.

Additional information

Supplementary information is available for this paper at https://doi.org/10.1038/s43246-020-00086-y.

Correspondence and requests for materials should be addressed to C.-W.Y., G.Y. or S.K.